Article

The International Journal of Robotics Research
2017, Vol. 36(3) 355–375

DOI: 10.1177/0278364917694428
journals.sagepub.com/home/ijr

Design, control, and testing of a thumb exoskeleton with series elastic actuation

Priyanshu Agarwal, Youngmok Yun, Jonas Fox, Kaci Madden, and Ashish D Deshpande

Abstract

We present an exoskeleton capable of assisting the human thumb through a large range of motion. Our novel thumb exoskeleton has the following unique features: (i) an underlying kinematic mechanism that is optimized to achieve a large range of motion, (ii) a design that actuates four degrees of freedom of the thumb, and (iii) a series elastic actuation based on a Bowden cable, allowing for bidirectional torque control of each thumb joint individually. We present a kinematic model of the coupled thumb exoskeleton system and use it to maximize the range of motion of the thumb. Finally, we carry out tests with the designed device on four subjects to evaluate its workspace and kinematic transparency using a motion capture system and torque control performance. Results show that the device allows for a large workspace with the thumb, is kinematically transparent to natural thumb motion to a high degree, and is capable of accurate torque control.

Keywords

Thumb exoskeleton, torque control, series elastic actuator, kinematic transparency, workspace analysis

1. Introduction

Stroke is a leading cause of serious long-term disability in the USA. Statistics reveal that there are an estimated total of 797,000 strokes per year in the USA, which amounts to an average of one stroke every 40 s (Mozaffarian et al., 2015). A stroke often affects one side of the body, with persistent impairment of an upper limb (Broeks et al., 1999; Doolittle, 1988). Another study showed that over 19.9 million people in the USA alone exhibit impaired physical function of the upper body and have difficulty in lifting or grasping (Brault, 2012). A disability of the upper extremity limits functional independence in activities of daily living and significantly deteriorates the quality of life of the affected individual (Williams et al., 1999). Rehabilitation using robots could help in providing intensive therapeutic exercises while also allowing for quantitative assessment of the recovery.

The literature shows that for rehabilitation robots, force-control-based strategies can be more effective for recovery of both the upper (Blank et al., 2014; Colombo et al., 2005; Pehlivan et al., 2014) and lower (Cai et al., 2006; Marchal-Crespo and Reinkensmeyer, 2009) limbs than pure position-based control (Harwin et al., 1995). This is because force-control-based strategies allow for safe and comfortable interaction and can be designed to encourage subject involvement. Such a therapy is shown to be more effective than passive motor training, even for a longer duration (Lotze et al., 2003), and is considered to be essential for provoking motor plasticity (Perez et al., 2004). Position-control-based strategies, however, physically guide the movement of the impaired limb to follow a predefined trajectory without enabling the subject to participate in the task actively (Bernhardt et al., 2005) or allowing for any subject-specific customization of the assistance (Meng et al., 2015). The guidance hypothesis in motor control research suggests that such a physically guided movement might decrease motor learning for some tasks, due to a reduction in burden (motor output, effort, energy consumption, or attention) on the subject's motor system, which is needed to discover the principles necessary to perform the task successfully (Schmidt and Bjork, 1992). Furthermore, some hand disabilities (e.g. spasticity) lead to uncertain motion of the digits. This uncertainty requires that appropriate forces are applied on the digits during rehabilitation therapy; simply moving the digits through some predetermined positions can lead to the application of large forces and further harm the hand.

The thumb provides more than 40% of the entire hand function and is given the first priority for replantation (Soucacos, 2001). Studies in understanding and classifying human hand use in activities of daily living have shown

Mechanical Engineering Department, University of Texas at Austin, USA

Corresponding author:
Ashish D Deshpande, Mechanical Engineering Department, University of Texas at Austin, TX-78712, USA.
Email: ashish@austin.utexas.edu

that, apart from the three flexion–extension joints, namely the carpometacarpal (CMC), metacarpophalangeal (MCP), and interphalangeal (IP) joints, thumb abduction–adduction at the CMC joint plays a significant role in accomplishing different types of grasp, including power, tripod, precision, palmar, tip pinch and lateral pinch (Dollar, 2014; Lin et al., 2011). Thumb opposition, which is vital for normal hand function, is achieved via coordinated flexion–extension and abduction–adduction motion at the CMC joint (Li and Tang, 2007). Furthermore, thumb abduction–adduction at the CMC joint has a large range of motion (40–45°) (Cooney et al., 1981; Smutz et al., 1998). Considering all these factors, we aim for the active rehabilitation of thumb flexion–extension at the CMC, MCP, and IP joints and abduction–adduction at the CMC joint as the design goal for our thumb exoskeleton.

A survey of existing thumb exoskeletons reveals that none of them allow for bidirectional torque control of the thumb joints individually (Table 1). Active bidirectional support is necessary for thumb joints in a rehabilitation setting for recovering pathological joints. Joint mobilization involves actively assisting the movement of the thumb joints in both directions (Villafañe et al., 2013). Specifically, we target neuromuscular impairments caused by stroke and spinal cord injury. These impairments often lead to the development of spasticity at the various upper limb joints (shoulder, elbow, and wrist), which causes pain even with passive stretching in a large majority of subjects (Wissel et al., 2010) and limited range of motion in the upper extremity (Beebe and Lang, 2009; Sukal et al., 2007). This indicates that the device should not significantly constrain the hand in a specific orientation during operation. In addition, individual control of the thumb joints is needed in order to provide therapy to a specific joint in certain thumb pathologies (e.g. spasticity). Furthermore, some studies of robot-assisted motor learning have shown that anatomical breakdown (independent motion of different joints) is more efficacious than complex arm movement for learning new motions (Klein et al., 2012). Moving each thumb joint individually could result in similar benefits for rehabilitation. This requires a device capable of assisting each thumb joint independently.

Based on the aforementioned considerations, our goal is to design a thumb exoskeleton with the following objectives.

1. The device should allow for accurate and stable bidirectional torque control of each thumb joint individually.
2. The design should be kinematically compatible with the human thumb and allow for flexion–extension motion at the CMC, MCP, and IP joints and abduction–adduction motion at the CMC joint.
3. The design should allow for a large workspace with the thumb.
4. The device should be lightweight and allow free motion of the hand with little movement resistance during operation.

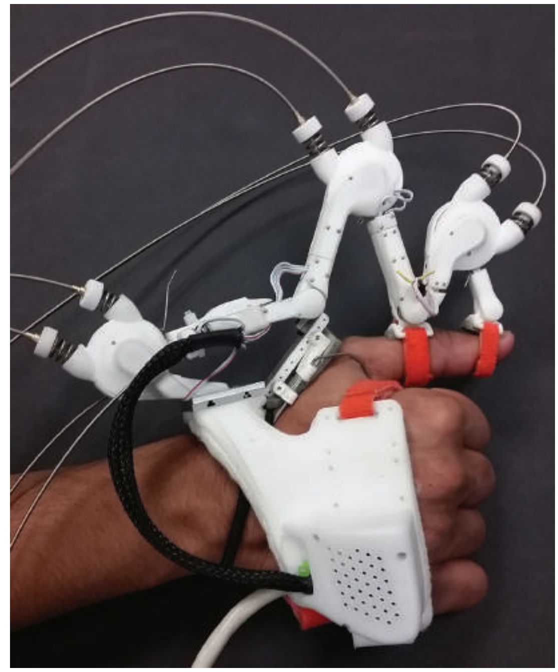

Fig. 1. Thumb exoskeleton prototype mounted on subject's hand for experimentation.

The rest of the paper is organized as follows. A detailed survey of existing thumb exoskeletons, along with their limitations, is presented in Section 2. The proposed kinematic mechanism of the thumb exoskeleton (Figure 1), the kinematics model, its optimization, and the prototype details are described in Section 3. Details of the torque controller implemented on the exoskeleton joints are presented in Section 4. Section 5 describes various experiments conducted to validate the workspace, kinematic transparency, and torque control of the device with human subjects; the results of these experiments are presented in Section 6. Finally, the paper concludes with a discussion and ideas for future work.

2. Background

Several thumb exoskeletons have been developed to date for rehabilitation, virtual reality, or teleoperation applications to allow for active actuation of the thumb (Table 1). For this review, we consider devices (a total of 16) that could actuate the thumb and are published in the literature with some experimental results. We compare the devices based on the following criteria, which are important for a thumb exoskeleton for rehabilitation:

(a) whether the device supports each thumb joint individually (exoskeletal type) or connects to the distal phalanx of the thumb (end-effector type);
(b) the number of active degrees of freedom (DOFs) in the device;
(c) the type of actuators used;
(d) whether the actuators are situated locally or remotely;

(e) the type of sensors in the device;
(f) the weight of the device;
(g) which physical quantities can be controlled using the device;
(h) the peak achievable force, pressure, or torque acting on the device.

Exoskeletal devices enable control of the position or torque applied at each joint explicitly, while end-effector type devices can only control the position or force at the distal phalanx. The number of active DOFs in a device determines the variety and complexity of the assisted motions that it can support. Individual assistance of the thumb joints is important in providing targeted therapy to specific joints, which may be necessary for certain thumb pathologies (e.g. spasticity). Ensuring natural coordinated motion at pathological thumb joints necessitates that the device be exoskeletal type with each DOF actuated individually. The type of actuator and its placement determine whether the device is bulky or light and, therefore, whether it will permit free movement of the hand while in operation. This is important for certain hand pathologies where the upper extremity cannot be oriented in certain manners. The types of sensor on the device determine what physical quantities the device can control. The weight of the device determines how easy or cumbersome it is to use. The controller on the device governs what physical quantities (position or force) the device can control, which in turn decides what robotic rehabilitation control paradigms (e.g. force-field control or assist-as-needed control (Marchal-Crespo and Reinkensmeyer, 2009)) the device is capable of rendering. Finally, the peak achievable forces or torques determine for what kind of impairments the device can be used. A limitation of the exoskeletons developed for virtual reality applications is that they only enable the application of unidirectional forces on the thumb. Rehabilitation exoskeletons are, however, required to apply bidirectional forces on the thumb due to the nature of the impairment. A comparison of the weight of the proposed thumb exoskeleton with existing exoskeletons shows that it has the least weight for the number of DOFs it offers. The weight per DOF for our device is about 34 g, which includes the weight of the exoskeleton-hand interface (Table 1).

Five main types of actuation mechanisms have been used for thumb exoskeletons:

(a) linkage-based actuation with a locally situated motor (Fontana et al., 2013; Garcia-Hernandez et al., 2014; Lambercy et al., 2013; Leonardis et al., 2015; Schabowsky et al., 2010; Ueki et al., 2012);
(b) tendon-based actuation with a locally situated motor (Avizzano et al., 2000; Hasegawa et al., 2008);
(c) cable and sheath transmission with remotely located motor (Aiple and Schiele, 2013; Cempini et al., 2015; DeSouza et al., 2014; Li et al., 2011; Sarakoglou et al., 2004);
(d) flexible shaft transmission with remotely located motor (Wang et al., 2011);
(e) pneumatic actuation (Bouzit et al., 2002; Takagi et al., 2009).

None of these mechanisms allows for accurate and stable torque control of the thumb joints individually. Furthermore, these mechanisms have poor back-drivability and result in a large reflected inertia. In addition, the transmission and actuator gearings in some of these mechanisms suffer from nonlinear friction and stiction, making it difficult to accurately control actuator torque or force.

The actuator mechanism of our thumb exoskeleton lies in category (c), so we discuss the designs in that category in more detail. A commercially available system, CyberGrasp (Aiple and Schiele, 2013; Bouzit et al., 2002), supports only one DOF motion of the thumb, controls a unidirectional phalanx force using motor current and cannot be used to control the position or forces of the thumb phalanges individually. The iHandRehab system (Li et al., 2011) is another hand exoskeleton with a thumb module that supports four DOFs of the thumb. However, experiments with this device revealed that significant friction (percentage of friction torque accounting for the driving torque is up to 95%) is present in the transmission. In addition, no control experiments were presented with this device. DeSouza et al. (2014) introduced a two-DOFs thumb exoskeleton, called IOTA (Isolated Orthosis for Thumb Actuation), for unidirectional actuation of the thumb. However, this device was only designed to control the positions of the joints. The HX device is another hand exoskeleton with a two-DOFs thumb module (Cempini et al., 2015). However, the flexion–extension motion at the MCP and IP joints is underactuated in this design and the device is designed to be position-controlled. Also, so far, Cempini et al. (2015) have only presented the design of the thumb module. Recently, Jo and Bae (2015) designed a hand exoskeleton with a thumb module utilizing a linear series elastic actuator (SEA) to control the grip force. However, this design has only one DOF for the thumb with no allowable abduction–adduction motion at the CMC joint. Also, Jo and Bae (2015) have presented only the results of preliminary test of the SEA; to our knowledge, no experiments with human subjects have been conducted with the device so far.

3. Design

In this section, we present the underlying mechanism of the proposed design, the kinematics of the coupled thumb exoskeleton system, kinematic optimization carried out to improve the range of motion of the design, details of the actuation mechanism for torque control, and, finally, the developed prototype.

Table 1. Comparison of characteristics and specifications of actuated thumb exoskeletons.[a]

Thumb exoskeleton	Physical characteristics						Specifications		Remarks
	Type	Active independent degrees of freedom	Actuator type	Actuation[b]	Sensors	Weight, g	Control[c]	Peak force, pressure, or torque	
Rutger's Master II (Bouzit et al., 2002)	End-effector	1[d] (CMC E, MCP E)	Pneumatic actuators with compressed air source	Remote, pneumatic tubes	Infrared reflective sensor for position, Hall effect angle sensor, pressure sensor	80[g]	Unidirectional phalanx force using pressure	16 N[f]	Designed for virtual reality applications
Hasegawa et al. (2008)	Exoskeletal	2[d]	DC motor + gear drive	Local, tendon	Potentiometer, encoder, electromyograph	—	Position or grasping on–off	—	Thumb opposition and IP + MCP joint are each actuated by one actuator.
Takagi et al. (2009)	Exoskeletal	1 (MCP F/E)	Air cylinder with compressed air source	Remote, pneumatic tubes	Bend sensor, electric pressure regulator	—	Grasping on–off	—	Experimental evaluation with wooden hand model is presented
HEXORR (Schabowsky et al, 2010)	End-effector	1 (CMC F/E)	AC servomotor + harmonic drive (100:1)	Local, linkage	Encoder, torque sensor	—	—	—	Hand is fixed in device; CMC A/A angle is adjustable
iHandRehab (Li et al., 2011)	Exoskeletal	4 (CMC F/E, CMC A/A, MCP F/E, IP F/E)	DC motor + capstan drive (8:1)	Remote, cable + sheath	Potentiometer, force sensor	250[e]	—	—	Significant losses (≈95%) observed in transmission
Wang et al. (2011)	Exoskeletal	5 (CMC F/E, CMC A/A, MCP F/E, MCP A/A, IP F/E)	RC servomotor	Remote, flexible shafts	Potentiometer, strain gauge	200	Position	±2.5 Nm	Significant losses observed in transmission
Ueki et al. (2012)	Exoskeletal	4 (CMC F/E, MCP F/E, IP F/E, opposition)	DC servomotor	Local, linkage	Encoders, 3-axis force sensors	—	Position	±3.72 Nm	Hand fixed in device
CyberGrasp (Aiple and Schiele, 2013; Bouzit et al, 2002)	End-effector	1[d] (CMC E, MCP E, IP E)	Servomotor	Remote, cable + sheath	Position	539[g]	Unidirectional phalanx force using motor current	12 N[f]	Losses in transmission are neglected
Avizzano et al. (2000); Fontana et al. (2013)	End-effector	3[d]	—	Local, linkage	—	510	Three-dimensional tip force	5 N	Distal and middle exoskeleton phalanx are coupled

Continued

Table 1. Continued.

	Physical characteristics						Specifications		
Thumb exoskeleton	Type	Active independent degrees of freedom	Actuator type	Actuation[b]	Sensors	Weight, g	Control[c]	Peak force, pressure, or torque	Remarks
Lambercy et al. (2013)	Exoskeletal	1[d] (CMC A/A)	Linear servomotor	Local, linkage	Single axis force sensor	126	Position	10 N[e]	
IOTA (isolated orthosis for thumb actuation) (DeSouza et al., 2014)	End-effector	2 (CMC A/A, MCP F/E)	Servomotor	Remote, cable + sheath	Encoder, bend sensor	230	Position	±0.384 Nm	Pediatric disorders
Maeder-York et al. (2014)	Exoskeletal	1[d] (CMC F/E, MCP F/E, IP F/E)	Fluidic actuator + compressor	Remote, pneumatic tubing	—	200	Grasping on–off	345 kPa	No CMC A/A motion supported
Garcia-Hernandez et al. (2014)	End-effector	1[d]	—	Local, linkage	—	—	Unidirectional force	3 N[f]	No experiments with thumb module are presented
Jo and Bae (2015)	Exoskeletal	1[d] (CMC F/E, MCP F/E, IP F/E)	Linear SEA with linear motor	Local, linkage	Potentiometer	298[g]	Grip force (only preliminary SEA testing presented so far)	9 N[f]	No CMC motion supported
HX (Cempini et al., 2015)	Exoskeletal	2[d] (MCP F/E, IP F/E, opposition)	DC motor + gear drive (14:1)	Remote, cable + sheath	—	270[h]	—	—	No experiments with thumb module presented
BRAVO (Leonardis et al., 2015)	Exoskeletal	1[d] (MCP F/E, IP F/E)	DC motor + gear drive	Local, linkage	Electromyograph, sensorized object pressure	950[e]	Position	±30 N	Designed for grasping of cylindrical objects
Proposed	Exoskeletal	4 (CMC F, MCP F, IP F)	SEA with DC motor + gear drive (14:1)	Remote, cable + sheath	Magnetoresistive angle sensor, potentiometer, encoder	136[i]	Torque	±0.3 Nm	Accurate torque control of individual thumb joint can be achieved

A/A: abduction–adduction; CMC: carpometacarpal; E: extension; F/E: flexion–extension; IP: interphalangeal; MCP: metacarpophalangeal; SEA: series elastic actuator.

[a] There is also a commercially available hand exoskeleton system, Festo ExoHand, with a thumb module having two degrees of freedom. However, limited published information is available on the device. Regardless, it cannot control the flexion–extension motion at the carpometacarpal, metacarpophalangeal, and interphalangeal joints independently.

[b] Actuation indicates whether the actuator was located at the joint (local) or remotely (remote) and the transmission mechanism.

[c] Missing control indicates that only mechanical design has been presented so far.

[d] Coupled actuation of degrees of freedom present in design.

[e] Combined weight of index finger and thumb exoskeleton (only moving parts).

[f] Only allows for unidirectional force.

[g] Total weight of hand exoskeleton.

[h] Force at thumb tip.

[i] Includes weight of hand base, which is 30 g.

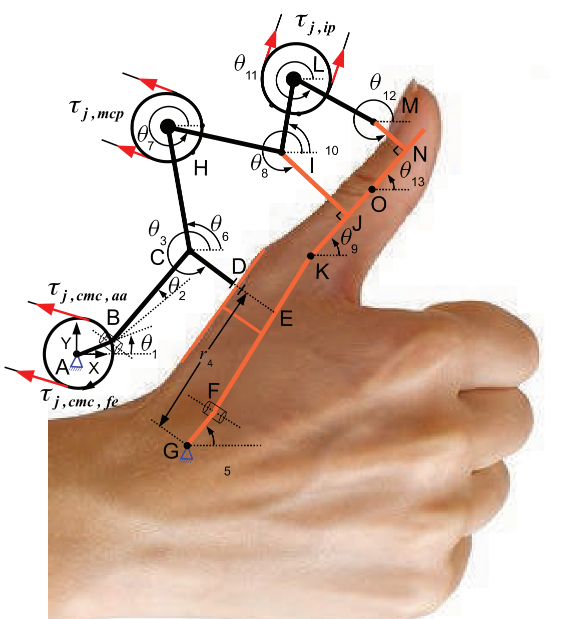

Fig. 2. Nomenclature for kinematic model of designed thumb exoskeleton. All angles are measured in a counterclockwise direction. Arrows in red depict forces acting on the system. E: location of intersection of line CD with center line of metacarpal bone of thumb. F, G: locations of carpometacarpal abduction–adduction and carpometacarpal flexion–extension joint of the thumb, respectively. H: location of actuated joint of exoskeleton for the metacarpophalangea flexion–extension degree of freedom. r_4: sliding length of slider from carpometacarpal flexion–extension axes. θ and θ_r: absolute and relative angles between the links participating in a joint, respectively. (x_G,y_G): coordinates of human carpometacarpal flexion–extension joint (point G) in the coordinate frame located at the exoskeleton joint at A. $l_{AC}(\theta_2)$: effective length of link AC. l_{CE}: length of link CE.

3.1. Mechanism

The human thumb consists primarily of four DOFs, namely, carpometacarpal flexion–extension (CMC FE), carpometacarpal abduction–adduction (CMC AA), metacarpophalangeal flexion–extension (MCP FE), and interphalangeal flexion–extension (IP FE). The mechanism for the thumb exoskeleton consists of three closed-loop chains to actuate these four DOFs while avoiding the exoskeleton–human joint axis misalignment problem (Figure 2). The CMC chain consists of four revolute joints and one prismatic joint, forming a closed-loop chain with the thumb carpometacarpal bone, allowing for two DOFs in the chain. The use of a sliding joint as the interaction interface between the exoskeleton and the thumb ensures that only normal forces are applied on the phalanx. One of the revolute joints enables thumb abduction–adduction motion. Both the MCP and IP chains consist of four revolute joints; these provide one DOF to each chain.

3.2. Kinematics

As a first step, we model the kinematic relationship between the actuated exoskeleton joint angles, and the thumb and passive exoskeleton joint angles. The kinematics of the thumb have been modeled in the past using intersecting or nonintersecting, orthogonal or nonorthogonal axes at the CMC joint (see, e.g. Bianchi et al., 2013; Chang and Pollard, 2008; Gabiccini et al., 2013). For our analysis, we assume that the exoskeleton and thumb abduction–adduction axes are instantaneously parallel to each other at each flexion angle, to avoid overconstraining the system, and that the two axes are orthogonal. Regardless, the kinematics of the device does not overconstrain the abduction–adduction motion of the thumb and it is difficult to capture the complex nature of the CMC joint in the coupled thumb exoskeleton model.

To determine the kinematic relationships of the CMC, MCP, and IP chains, each of the chains is considered as a four-bar mechanism. We analyzed the thumb and exoskeleton as a planar system for each CMC abduction–adduction angle. This is a reasonable assumption for our purposes; moreover, the kinematic parameters (e.g. location and orientation of the CMC FE and CMC AA axes, orientation of the exoskeleton links with respect to the thumb joints) necessary for a three-dimensional analysis are almost impossible to measure in a subject.

For the CMC chain, since the motion at the CMC abduction–adduction joint is out of plane, an equivalent four-bar mechanism is realized that takes into account the changing length of the link AC due to abduction–adduction motion. The loop closure equation for the proximal (CMC) chain of the thumb exoskeleton (Figure 2) is then given by

$$l_{AC}(\theta_2)\,\mathrm{e}^{\mathrm{i}\theta_1} + l_{CE}\mathrm{e}^{\mathrm{i}\theta_3} + r_4\mathrm{e}^{\mathrm{i}(\theta_5-\pi)} = x_G + \mathrm{i}y_G \qquad (1)$$

where $l_{AC}(\theta_2)$ is the effective length of the link AC in the CMC four-bar chain, which is a function of the CMC AA angle (θ_2); l_{CE} is the length of line segment CE; r_4 represents the sliding length in the CMC chain at a given configuration; θ and θ_r represent the absolute and relative joint angles between the links participating in a joint, respectively; (x_G, y_G) represent the coordinates of the human CMC FE joint (point G) in the coordinate frame located at the exoskeleton joint at A. The loop closure equations for the middle (MCP) and distal (IP) chains are expressed in a similar way.

The forward kinematics deals with evaluation of the thumb CMC, MCP, and IP joint angles (θ_5, θ_9, θ_{13}) and the exoskeleton passive joint displacements (r_4, θ_6, θ_{10}) given the exoskeleton relative joint angles (θ_{1r}, θ_{7r}, θ_{11r}). The relative joint angle is the angle measured by the angle sensor mounted at the joint. The kinematics of the system are solved using the standard four-bar kinematics solution (Norton, 1999) in the order: CMC, MCP, IP. If the loop closure equation (1) results in significant residual owing to an error in geometric parameter measurement, we evaluate the least-squares solution of the equation. The final solution can be expressed as

$$\mathbf{X} = \mathbf{X}(\Theta_{\mathbf{r}}) \tag{2}$$

where

$$\mathbf{X} = \begin{bmatrix} r_4 & \theta_5 & \theta_9 & \theta_{13} \end{bmatrix}^{\mathrm{T}}$$

and

$$\mathbf{\Theta_r} = \begin{bmatrix} \theta_{1\mathrm{r}} & \theta_{2\mathrm{r}} & \theta_{7\mathrm{r}} & \theta_{11\mathrm{r}} \end{bmatrix}^{\mathrm{T}}$$

3.3. *Kinematics optimization*

A thumb exoskeleton that allows for a large range of motion for different hand sizes could serve a variety of target populations with minimal customization. Moreover, a design that results in increased mechanical advantage from the exoskeleton joint to the human joint would reduce the torque requirement at the exoskeleton joint and thus help in reducing the size of the exoskeleton pulley and Bowden cable. To this end, our goal is to maximize the range of motion and mechanical advantage by choosing appropriate values for the kinematic parameters (link lengths and location of exoskeleton CMC FE joint) of the design. We also consider two different hand sizes (thin and thick) to understand the effect of design parameters on the two objectives for different hand sizes. We focus on the CMC chain of the exoskeleton, as several feasible solutions could easily be obtained for the MCP and IP chains without explicitly setting up an optimization study.

To determine the mechanical advantage for CMC flexion–extension motion, we take the differential of the kinematic equation of the CMC chain (1) and solve for $\delta\theta_1$ and δr_4, resulting in

$$\begin{bmatrix} -l_{\mathrm{AC}}(\theta_2)\sin\theta_1 & \cos\theta_5 \\ l_{\mathrm{AC}}(\theta_2)\cos\theta_1 & \sin\theta_5 \end{bmatrix} \begin{bmatrix} \delta\theta_1 \\ \delta r_4 \end{bmatrix} = \begin{bmatrix} l_{\mathrm{CE}}\sin\theta_3 + r_4\sin\theta_5 \\ -l_{\mathrm{CE}}\cos\theta_3 - r_4\cos\theta_5 \end{bmatrix} \delta\theta_5 \tag{3}$$

The mechanical advantage in flexion–extension at the CMC joint is then evaluated as $\eta = \delta\theta_1/\delta\theta_5$. An optimization analysis is set up to maximize the range of motion at the CMC chain while also maximizing the mechanical advantage (equation (4)). Also, since the CMC joint has a higher extension range of motion than flexion, we constrained the lower and upper limits of the angle

$$\begin{aligned} &\max_{\mathbf{P}} \left(\theta_{5,\max}(\mathbf{P}) - \theta_{5,\min}(\mathbf{P}), \eta(\mathbf{P})\right) \\ &\text{s.t. } \theta_{5,\max} \geq \theta_{5,\mathrm{u}} \\ &\quad\ \theta_{5,\min} \leq \theta_{5,\mathrm{l}} \\ &\quad\ r_{4,l} \leq r_4 \leq r_{4,\mathrm{u}} \\ &\quad\ \mathbf{P}_{\mathrm{l}} \leq \mathbf{P} \leq \mathbf{P}_{\mathrm{u}} \end{aligned} \tag{4}$$

where $\theta_{5,\max}$ and $\theta_{5,\min}$ refer to the maximum and minimum CMC flexion angles, respectively; $\theta_{5,\mathrm{u}}$ and $\theta_{5,\mathrm{l}}$ are the upper and lower limits, respectively, of θ_5 that a feasible solution must achieve; $r_{4,\mathrm{u}}$ and $r_{4,\mathrm{l}}$ are the upper and lower bounds, respectively, of r_4 that a feasible solution must satisfy; and $\mathbf{P} = \begin{bmatrix} x_{\mathrm{G}} & y_{\mathrm{G}} & l_{\mathrm{AC}} & l_{\mathrm{CD}} \end{bmatrix}^{\mathrm{T}}$ are the design variables to be determined that satisfy the optimization criteria. Note that $(x_{\mathrm{G}}, y_{\mathrm{G}})$ is used as a design variable since a change in the location of the coordinate frame at point A changes the coordinates of point G (Figure 2).

Since equation (4) is a multi-objective optimization problem with nonlinear objective functions, we used parametric analysis to determine the best feasible solution for the problem. We varied the design variables throughout the design space and evaluated the range of motion and mechanical advantage for small and large hand sizes for each design configuration. The baseline subject was chosen based on the thumb size closest to the 50th percentile of the British adult male population, for ages between 19 and 65 years (Smith, 2008) and the subject with a thicker thumb was chosen based on the thumb size closest to the 95th percentile of the same population. We considered a set of six values for each variable, which resulted in a total of $(6 \times 6 \times 6 \times 6 =)$ 1296 models, which were created and compared for the optimum solution. We favored solutions that resulted in a larger range of motion. For solutions that resulted in the same range of motion, we chose those that maintained the range of motion across all hand sizes. The four parameters were varied in the ranges

$$\begin{aligned} x_{\mathrm{G}} &\in [0.0092, 0.0692]\mathrm{m} \\ y_{\mathrm{G}} &\in [-0.0925, -0.0725]\mathrm{m} \\ l_{\mathrm{AC}} &\in [0.0725, 0.1675]\mathrm{m} \\ l_{\mathrm{CD}} &\in [0.0225, 0.05]\mathrm{m} \end{aligned}$$

The analysis resulted in several different solutions with different upper and lower limits on the CMC flexion–extension angle (Figure 3). The results showed that solutions with higher ranges of motion tend to have lower mechanical advantages. For example, the solutions with ranges of motion of 43° and 44° have maximum mechanical advantages of 0.83 and 0.67, respectively. For all the solutions, the ranges of motion reduces as the CMC abduction–adduction angle increases. For example, the ranges of motion reduced from 43° to 41° and from 35° to 34° for the no-abduction full-abduction positions with thinner and thicker hands, respectively, for one solution. However, the CMC flexion–extension range of motion of the human thumb also decreases as the CMC abduction–adduction angle increases. In addition, the range of motion is adversely affected as the size (thickness) of the metacarpal bone increases while keeping the available sliding length constant. Furthermore, solutions that are better in terms of range of motion are also more robust to changes in thumb thickness variation. For example, the range of motion changes from 44° and 43° to 36° and 35°, respectively, for thinner to thicker hands. The results also showed that the range of motion in the CMC chain is particularly sensitive to l_{CD}. Smaller values of l_{CD} resulted in larger ranges of motion for hands of different thicknesses in both unabducted and abducted positions. We chose the solution that maximized the range of motion over the one that maximized mechanical advantage, as reduced range of motion limits functionality whereas reduced mechanical advantage merely increases the forces and torques acting on the system by a small magnitude. The final parameter values of $x_G = 0.0392$, $y_G = -0.065$, $l_{AC} = 0.10$, and $l_{CD} = 0.0225$ resulted in the maximum range of motion of 44° and a mechanical advantage varying from 0.32 to 0.72 for the corresponding range of motion.

3.4. Actuation

Miniature SEAs based on Bowden cables are used to control the torque of each exoskeleton joint. These actuators are highly back-drivable with low reflected inertia and a weight of around 30 g each (Agarwal et al., 2015). Each actuated joint consists of a pulley with a cable attached to the circumference of the pulley. The Bowden cable consists of a metal sheath with a stainless steel wire rope to allow for transmission of the required mechanical power to the device. For each end of the Bowden cable connected to the joint pulley, there is a compression spring attached to the Bowden cable sheath. Introduction of the series elastic element in the transmission mechanism provides a means of accurately estimating the cable tension from joint displacement measurements obtained using the joint angle sensor and the motor encoder. Since the elastic element is located at the exoskeleton end, the significant friction losses that exist in the Bowden cable do not affect the torque estimates. We used brushed DC motors (20 W with a stall torque of 0.2 Nm) from Maxon, Inc. with a planetary gearhead of 111:1 reduction ratio as the actuators for our SEAs.

We carried out a thorough validation of the performance of the Bowden-cable-based SEAs including accuracy and fidelity of torque tracking, torque bandwidth, performance at different peak torques, performance under disturbance, dynamic range, and performance during interaction on a test rig using a six-axis load cell. For torque tracking performance, the estimated torque is compared with the measured torque to validate the accuracy and fidelity of torque tracking. The torque bandwidth of the SEA was evaluated using a linear chirp signal as the desired torque for the system. We evaluated the magnitude of the frequency response of the SEAs using the measured torque data by taking the fast Fourier transform of the commanded and measured torque, which provides an amplitude spectrum of the system input and output. The magnitude of the frequency response was evaluated as the ratio of the amplitude of the output to the input in the frequency domain.

Experiments show that the root mean square error for torque tracking at 0.5 Hz is 0.023 Nm (4.6% of peak torque) (Figures 4(a) and (b)). Furthermore, the measured joint torque to spring deflection variation is linear (Figure 4(c)). Performance characterization of the SEA shows that the actuator has adequate torque source quality (root mean square error $<$ 10% of peak torque) with high fidelity ($>$97% at 0.5 Hz torque, sinusoidal), force tracking bandwidth of 10 Hz (at 0.5 Nm peak torque) and peak torques of 0.7 Nm. Further details of different types of experiments conducted to validate the performance of the SEAs will be described elsewhere. These specifications satisfy the torque requirement (0.3 Nm maximum) for hand rehabilitation, as measured by experienced therapists through a torque measuring device (Ueki et al., 2012). In addition, the torque bandwidth of the human force compliance control loop of 1–2 Hz (Chan and Childress, 1990; Sheridan and Ferrell, 1974) is met by the actuator.

3.5. Prototype

The optimized kinematic mechanism of the thumb exoskeleton is realized in the form of a prototype (Figure 5). The SEAs are implemented at the four actuated joints of the exoskeleton. At the CMC joint, the SEAs are implemented for both the flexion–extension and the abduction–adduction joint. This is achieved by mounting the SEA of the CMC AA joint to the output of the SEA of the CMC FE joint. The SEA is small enough (44 mm × 35 mm × 17 mm) that this is possible. Each joint has bearings to reduce friction at the joints. Each link is adjustable to allow for quick customization of the device for a specific subject. We use a magneto-resistive angle sensor (KMA210, NXP Semiconductors) with a diametrically magnetized ring magnet to measure the exoskeleton joint angles (enclosed in casings). Owing to the close proximity of the CMC FE and CMC AA joint axes, there is a possibility of interference in the measurements. To avoid this, we use a sliding-contact-type miniature rotary potentiometer to sense the joint angle at the CMC AA joint.

The thumb exoskeleton chain is mounted on a hand base with an adjustable mount that enables the angular and linear positions of the chain to be adjusted to accommodate different hand sizes. The sensor wires are routed internally to ensure a clear and robust design. The various parts of the exoskeleton are manufactured using selective laser sintering (Wikipedia, 2016) to keep the overall design light in weight. Some of the load-bearing parts (e.g. SEA pulleys, adjustable mount) are machined from metal (6061-T6 aluminum) to ensure durability of the device. The weight of the nonwearable parts, which includes the motors and their drivers, pulleys, cable tensioning mechanism, and the metal frame, is 4.6 kg. In the current stage of development, we focused on making the nonwearable parts highly modular but we have not focused on optimizing the design of these parts for weight.

A challenge in thumb exoskeleton design has been to apply bidirectional forces on the thumb metacarpal. This is because it is difficult to hold on to the metacarpal bone of the thumb as there is no circumferential access to it and the

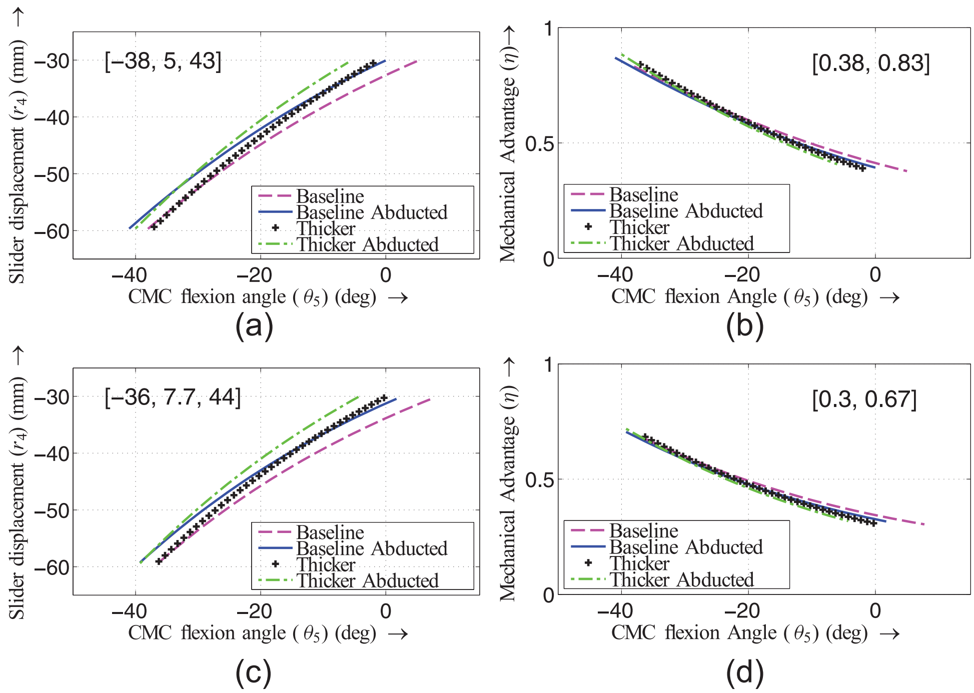

Fig. 3. Two best solutions from parametric study to maximize range of motion and mechanical advantage for flexion–extension motion at carpometacarpal (CMC) joint. Plots in the left and right columns show the slider displacement, which determines the flexion–extension range of motion at the carpometacarpal joint, and the corresponding mechanical advantage, respectively. Baseline and thicker: thinner and thicker hand metacarpal bones, respectively. Abducted: the solution in a fully abducted thumb position ($\theta_2 = 25°$). Values in square brackets in the left column are the minimum value, maximum value, and range of motion, respectively, of the flexion angle at the carpometacarpal joint for the baseline configuration of the solution. Values in square brackets in the right column are the minimum and maximum values, respectively, of the mechanical advantage for the baseline configuration of the solution.

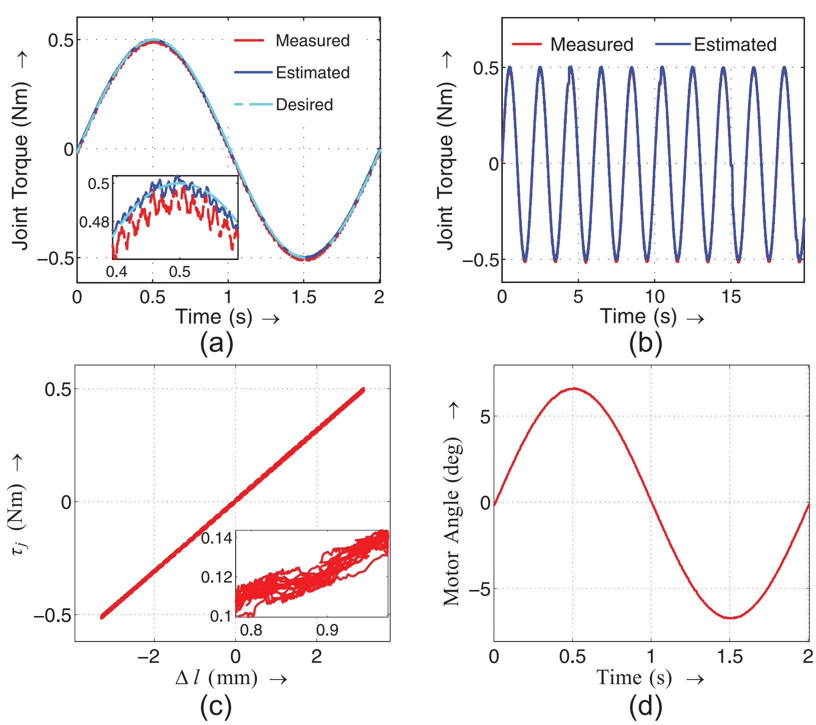

Fig. 4. Joint torque tracking performance of Bowden-cable-based SEA with sinusoidal desired torque trajectory. (a) Comparison of joint torque trajectory for one cycle; (b) comparison of joint torque trajectory for multiple cycles; (c) joint torque variation with spring deflection; (d) motor position input trajectory.

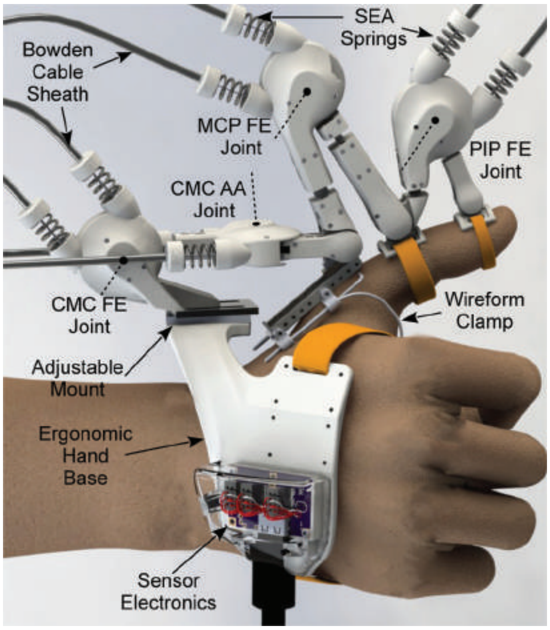

Fig. 5. CAD model of thumb exoskeleton prototype. AA: abduction–adduction; FE: flexion–extension; CMC: carpometacarpal; MCP: metacarpophalangeal; PIP: proximal interphalangeal; SEA: series elastic actuator.

muscle bellies of the thenar eminence change in shape as the thumb moves around. We designed an ergonomic wire form structure with galvanized steel wire to address this issue. The structure has a ring around the MCP joint with four protruding legs placed so as to produce minimal interference with any deformation of the muscles. The structure rests closely against the metacarpal, cages the metacarpal bone, and provides stability to transfer and distribute the forces applied by the exoskeleton on the metacarpal. The slider in the CMC chain is attached to the wireform structure with an adjustable mount to allow for the transmission of the forces from the exoskeleton to the metacarpal. The structure is kept in place with the help of an elastic band (not shown in figure), which prevents it from slipping forward when the forces are applied. This wireform design is a lightweight and comfortable solution to the challenging problem of exoskeleton attachment to the thumb.

4. Controls

A torque controller was implemented to track the desired torque trajectories at the exoskeleton SEA joints (Figure 6). The output of the system is the torque ($\hat{\mathbf{y}}$) generated at the exoskeleton joints through the SEA, as estimated using

$$\hat{\mathbf{y}} = \begin{bmatrix} \tau_{\mathrm{j,cmc,fe}} \\ \tau_{\mathrm{j,cmc,aa}} \\ \tau_{\mathrm{j,mcp}} \\ \tau_{\mathrm{j,ip}} \end{bmatrix} = 2\mathbf{K}r_{\mathrm{j}}\left(r_{\mathrm{m}}\boldsymbol{\Theta}_{\mathrm{m}} - r_{\mathrm{j}}\left(\boldsymbol{\Theta}_{\mathrm{r}} - \boldsymbol{\Theta}_{\mathbf{r0}}\right)\right) \quad (5)$$

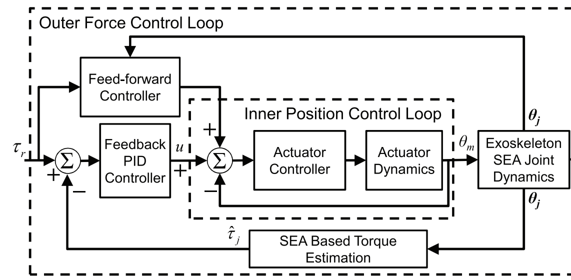

Fig. 6. Torque controller for series elastic actuators. The inner position control loop represents the position control implemented in the motor driver. The outer force control loop refers to the control loop implemented for output torque tracking. PID: proportional–integral–derivative.

where

$$\mathbf{K} = \begin{bmatrix} k_{\mathrm{j,cmc,fe}} & 0 & 0 & 0 \\ 0 & k_{\mathrm{j,cmc,aa}} & 0 & 0 \\ 0 & 0 & k_{\mathrm{j,mcp}} & 0 \\ 0 & 0 & 0 & k_{\mathrm{j,ip}} \end{bmatrix}$$

$$\boldsymbol{\Theta}_m = \begin{bmatrix} \theta_{\mathrm{m,cmc,fe}} \\ \theta_{\mathrm{m,cmc,aa}} \\ \theta_{\mathrm{m,mcp}} \\ \theta_{\mathrm{m,ip}} \end{bmatrix}$$

$k_{\mathrm{j,cmc,fe}}$, $k_{\mathrm{j,cmc,aa}}$, $k_{\mathrm{j,mcp}}$, and $k_{\mathrm{j,ip}}$ represent the magnitude of the effective stiffness at the exoskeleton CMC FE, CMC AA, MCP, and IP joints, respectively, and $\theta_{\mathrm{m,cmc,fe}}$, $\theta_{\mathrm{m,cmc,aa}}$, $\theta_{\mathrm{m,mcp}}$, and $\theta_{\mathrm{m,ip}}$ are the CMC FE, CMC AA, MCP, and IP motor angles, respectively. The feed-forward proportional–integral–derivative controller is then given by

$$\begin{aligned} \mathbf{e} &= \mathbf{y}_d - \hat{\mathbf{y}} \\ \dot{\mathbf{e}} &= \dot{\mathbf{y}}_d - \dot{\hat{\mathbf{y}}} \\ \mathbf{u} &= \frac{1}{r_m}\left(\frac{\mathbf{K}^{-1}\mathbf{y_d}}{2r_j} + r_j\left(\boldsymbol{\Theta}_r - \boldsymbol{\Theta}_{\mathbf{r0}}\right)\right) + \mathbf{K_p}\mathbf{e} \\ &\quad + \mathbf{K_d}\dot{\mathbf{e}} + \mathbf{K_i}\int \mathbf{e}dt \end{aligned} \quad (6)$$

where $\mathbf{e}$ is the vector containing exoskeleton joint torque errors, $\mathbf{y}_{\mathrm{d}}$ is the vector containing the desired torque at the two exoskeleton joints, and $\mathbf{u}$ is the control input vector (desired motor position) for the four exoskeleton joints. $\mathbf{K_p}$, $\mathbf{K_d}$, and $\mathbf{K_i}$ represent the diagonal gain matrices for the proportional–integral–derivative controller.

5. Experimentation

To examine the effectiveness of the thumb exoskeleton in achieving our design goals, we conducted experiments with the prototype to assess (i) the workspace of the thumb with and without the exoskeleton, (ii) the kinematic transparency of the device to understand how the natural motion of the thumb is affected by the device, and (iii) the torque control of the device. Four healthy subjects (three men and one

Table 2. Comparison of thumb anthropometric parameters of human subjects participating in experiments.

Subject	Thumb length,[a] mm	Thumb breath,[b] mm	Thumb thickness,[c] mm
I	53	23	29
II	59	26	36
III	56	25	34
IV	50	23	28

[a] Length from metacarpophalangeal joint to tip of thumb.
[b] Width of thumb at metacarpophalangeal joint.
[c] Thickness of thumb at middle of thumb metacarpal bone.

woman, aged 20–33 years), with no history of any neuromuscular injury, voluntarily participated in the experiments after providing informed consent. The anthropometric measurements of the thumbs of the four subjects are presented in Table 2. The study was approved by the institutional review board of The University of Texas at Austin.

For the workspace and kinematic transparency experiments, motion capture data were recorded using an active marker motion capture system (PhaseSpace Inc.) at 480 Hz similar to the one used by Bianchi et al. (2013) and Gabiccini et al. (2013). Markers can be placed on the joints (Cerveri et al., 2007; Choi, 2008; Metcalf et al., 2008; Zhang et al., 2003) or between the joints (Chang and Pollard, 2008; Miyata et al., 2004). The location of the motion capture markers in our study was chosen to ensure minimal interference with the exoskeleton attachment interface (Figure 7) and maintain similar experimental conditions without and with the device. Three markers were placed on the wrist to establish a coordinate frame to account for any movement of the hand. The remaining four markers were placed at each of the three joints and the tip of the thumb. The subject's hand was supported to ensure minimal motion at the wrist joint. Since, these experiments were intended only to characterize the kinematics of device, the Bowden-cable-based SEAs were not connected.

5.1. Workspace analysis

To quantify the volume of the workspace of the thumb with the human subjects, we carried out experiments using the motion capture system. We asked the subjects to move their thumb to reach full achievable range of motion at each joint. To capture the curvature of the workspace boundary accurately, several repetitions of the motion were performed. These experiments were carried out both without and with the exoskeleton. The collected data were then processed to correct for any overall hand movement using the three ground markers on the wrist. A convex hull was fitted to the data for markers 4, 5, 6, and 7 and was used to measure the volume of the region that the thumb was able to reach. The percentage volume of the workspace of the thumb with the exoskeleton with respect to without it (given in equation (7)) gives a measure of the volumetric range of motion preserved with the exoskeleton

$$\eta = \frac{V_{\mathrm{we}}}{V_{\mathrm{ne}}} \times 100\% \quad (7)$$

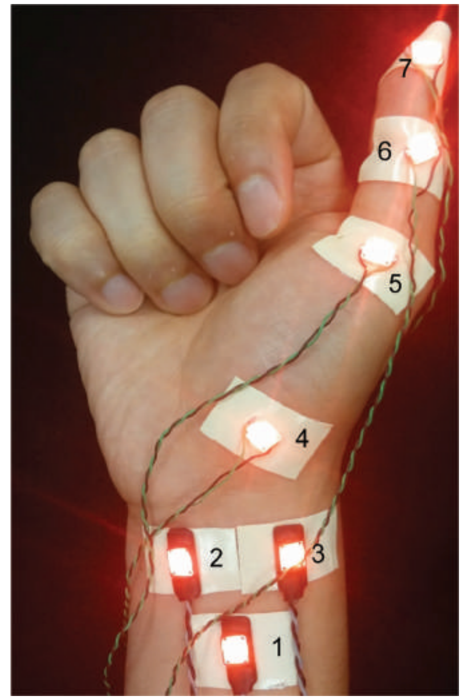

Fig. 7. Motion capture marker set used in kinematic experiments with thumb exoskeleton.

5.2. Kinematic transparency

Kinematic transparency tests were conducted to quantify the similarity of the motion without and with the thumb exoskeleton. We used the following protocol for the kinematic transparency experiments. The motion capture markers were placed on the thumb and the subjects were asked to perform four different motions at four different speeds:

(a) CMC, MCP, and IP joint articulation through the full active range of motion in flexion and extension, while maintaining the abduction–adduction angle at the CMC joint;
(b) full active range of abduction–adduction motion at the CMC joint while maintaining the position of the other joint angles;
(c) full active range of flexion–extension and abduction–adduction motion in a circular pattern at the CMC joint;
(d) full active range of flexion–extension motion at the MCP and IP joint while maintaining the position of the other joints.

The rationale behind choosing motion (a) rather than isolated motion at the CMC joint was that it was difficult for the subjects to achieve the full active range of motion without flexing the MCP joint. The subjects were asked to wear the device and the link lengths were adjusted to ensure that the subjects could achieve their full active range of motion with the device. Care was taken to ensure that the motion capture markers did not move while wearing the device. Enough time was provided to allow the subject to become comfortable with the device and practice each motion. The subjects were then asked to perform the same motions with the exoskeleton. The current paradigm of stroke rehabilitation to improve hand function is focused on high-intensity, repetitive, and task-specific training. However, there is no widely accepted protocol for hand rehabilitation after stroke, and the treatment varies in duration, intensity, and frequency (Sale et al., 2012). Rehabilitation exercises for the finger are typically carried out at angular velocities of 50°/s, i.e. full range of motion frequencies of 0.5 Hz (Adamovich et al., 2005; Kawasaki et al., 2006). To validate the performance of the device at different frequencies, the experiments were conducted at four different speeds, 0.25 Hz, 0.5 Hz, 0.75 Hz, and 1 Hz. An audio cue, with a metronome, was provided to help the subjects maintain the required finger frequency. The motion capture data were resampled at 1/10 frequency (48 Hz).

The motion capture data were processed to evaluate the angle of each phalanx with respect to the ground reference frame established using the markers placed on the wrist. The orientation of the ground reference frame was first calculated using Gram–Schmidt orthonormalization (Cheney and Kincaid, 2009) as

$$
\begin{aligned}
\mathbf{u}_x &= \mathbf{p}_3 - \mathbf{p}_2 & \hat{\mathbf{e}}_x &= \frac{\mathbf{u}_x}{||\mathbf{u}_x||} \\
\mathbf{u}_y &= \mathbf{p}_3 - \mathbf{p}_1 - \hat{\mathbf{e}}_x.(\mathbf{p}_3 - \mathbf{p}_1) & \hat{\mathbf{e}}_y &= \frac{\mathbf{u}_y}{||\mathbf{u}_y||} \\
\mathbf{e}_z &= \hat{\mathbf{e}}_x \times \hat{\mathbf{e}}_y
\end{aligned}
\tag{8}
$$

where $\mathbf{p}_i$ is the three-dimensional position of the ith marker in the reference frame of the motion capture system, $\mathbf{e}_x$, $\mathbf{e}_y$, and $\mathbf{e}_z$ refer to the unit vectors in the ground reference frame along the x-, y-, and z- axes, respectively, and $\mathbf{u}_x$ and $\mathbf{u}_y$ are the vectors evaluated to calculate the unit vectors. The rotation angles of the metacarpal phalanx in three dimensions were calculated with respect to the evaluated reference frame using direction cosines, as given in equation (9). Similarly the angles for the middle and distal phalanges were calculated using their respective markers.

$$
\begin{aligned}
\theta_{\mathrm{cmc},x} &= \cos^{-1}\left(\frac{(\mathbf{p}_5 - \mathbf{p}_4).\hat{\mathbf{e}}_x}{||(\mathbf{p}_5 - \mathbf{p}_4)||}\right) \\
\theta_{\mathrm{cmc},y} &= \cos^{-1}\left(\frac{(\mathbf{p}_5 - \mathbf{p}_4).\hat{\mathbf{e}}_y}{||(\mathbf{p}_5 - \mathbf{p}_4)||}\right) \\
\theta_{\mathrm{cmc},z} &= \cos^{-1}\left(\frac{(\mathbf{p}_5 - \mathbf{p}_4).\hat{\mathbf{e}}_z}{||(\mathbf{p}_5 - \mathbf{p}_4)||}\right)
\end{aligned}
\tag{9}
$$

Table 3. Thumb workspace analysis results without (V_{ne}) and with the device (V_{we}) for the different subjects.

Subject	V_{ne}, cm^3	V_{we}, cm^3	η
I	707.31	560.25	79.21%
II	1152.54	1049.86	91.09%
III	729.38	570.73	78.25%
IV	701.32	658.16	93.84%
Average			85.59%

5.3. Torque control

Torque control experiments were carried out to confirm that the device could track a desired torque trajectory using the controller proposed in Section 4. The same four subjects participated in these experiments. In the first phase of these experiments, the subjects were asked to avoid any voluntary contraction of the muscle and let the exoskeleton actively move their thumbs around. In the second phase, the subjects were asked to block the motion to validate whether the device still tracked the desired torque trajectory. We used a mean and phase-shifted sinusoidal trajectory as the desired torque trajectory at each joint of the thumb exoskeleton, as

$$
\begin{aligned}
\tau_{\mathrm{j},i} &= \tau_{\mathrm{A},i}\left(\sin(2\pi f t + \phi_{\tau,i}) + D_{\tau,i}\right) \times S(t) \\
S(t) &= \frac{1}{1 + \mathrm{e}^{-(t-5)}}
\end{aligned}
\tag{10}
$$

where $S(t)$ is the sigmoid function, which is multiplied to gradually increase the torque levels from zero to their respective values to ensure that any phase and amplitude relationship between the thumb torques can be achieved.

6. Results

6.1. Workspace analysis

Results showed that the exoskeleton is able to retain around 85.59% workspace on average (Table 3). In addition, some variability was observed in the percentage of reachable workspace from subject to subject. This variability might result from the significant natural variation that exists in thumb anatomy, which has been shown to support the idea of nonexistence of a single generic biomechanical model that can represent the entire population (Santos and Valero-Cuevas, 2006). A comparison of the workspace in the xy-, yz-, and xz- planes without and with the exoskeleton for Subject III shows that the major portion of the workspace can be reached with the exoskeleton (Figure 8).

6.2. Kinematic transparency

A comparison of the thumb phalanx angles in three dimensions without and with the exoskeleton was carried out for the different motions. The Pearsons product moment correlation coefficient averaged over three repetitions was calculated to quantify the degree of similarity between the angle

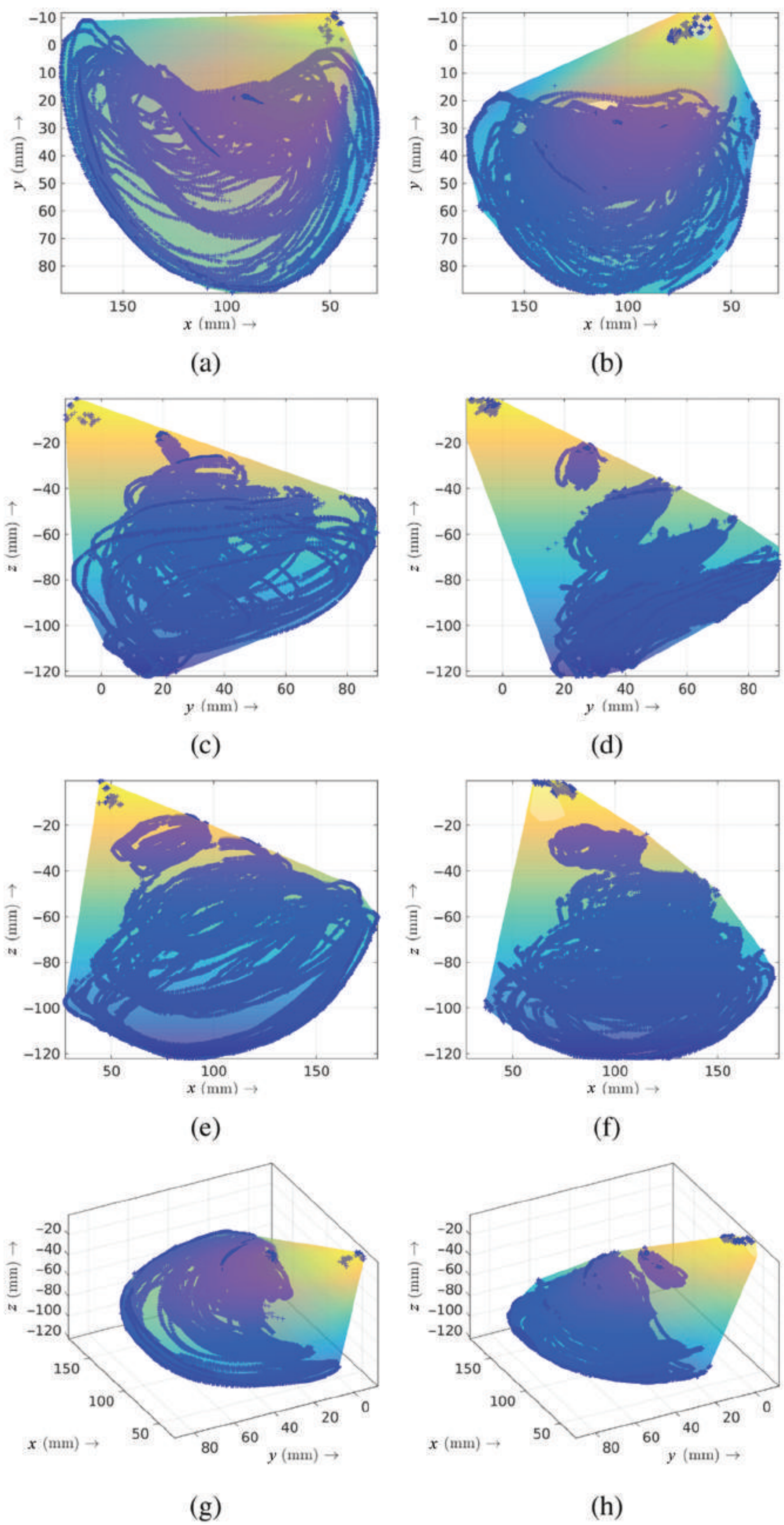

Fig. 8. Workspace results without and with the exoskeleton for Subject III. The left and right columns represent the plots of the thumb workspace without and with the thumb exoskeleton, respectively. Dark trajectories are the plotted marker data as captured using the motion capture system.

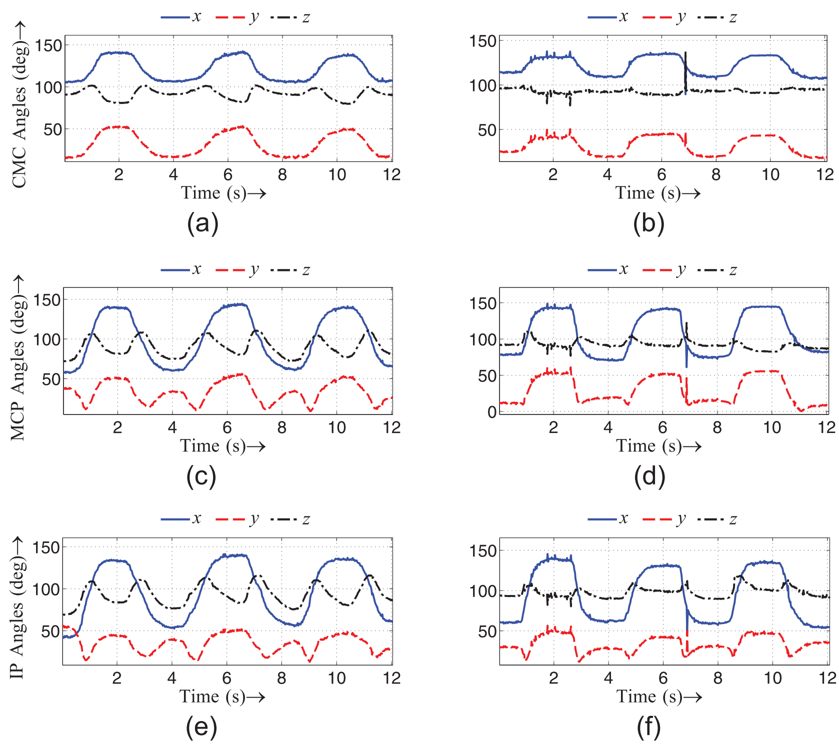

Fig. 9. Example trajectories from kinematic transparency tests without and with the exoskeleton for motion (a) at 0.25 Hz with Subject I. The left and right columns represent the plots of the various thumb phalanx angles with respect to the reference frame without and with the thumb exoskeleton, respectively.

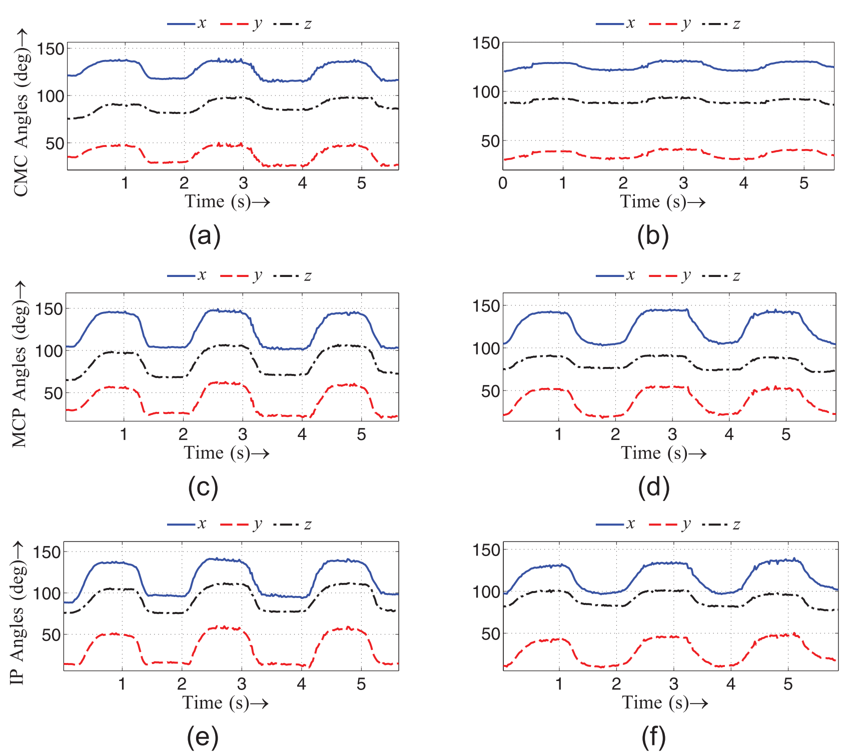

Fig. 10. Example trajectories from kinematic transparency tests without and with the exoskeleton for motion (b) at 0.5 Hz with Subject I. The left and right columns represent the plots of the various thumb phalanx angles with respect to the reference frame without and with the thumb exoskeleton, respectively.

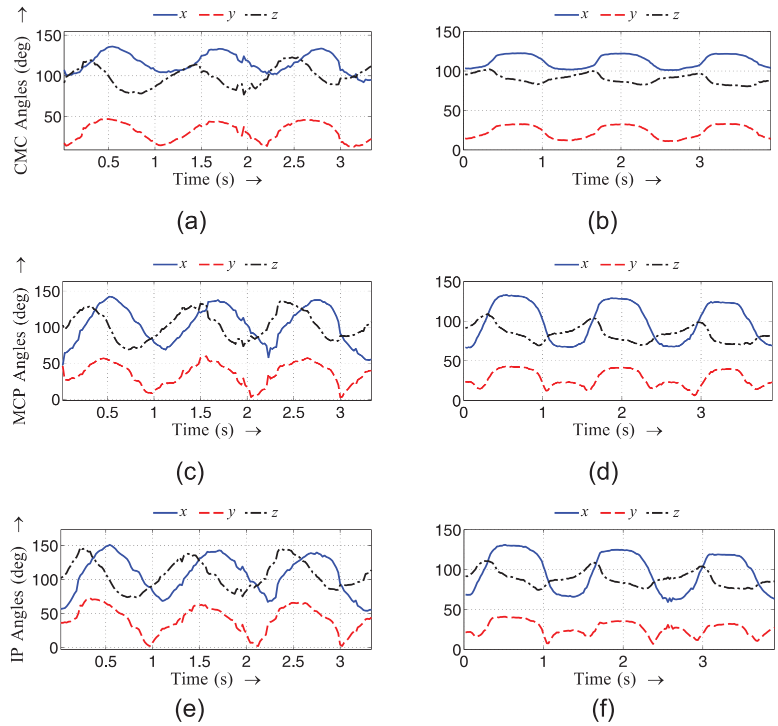

Fig. 11. Example trajectories from kinematic transparency tests without and with the exoskeleton for motion (c) at 0.75 Hz with Subject I. The left and right columns represent the plots of the various thumb phalanx angles with respect to the reference frame without and with the thumb exoskeleton, respectively.

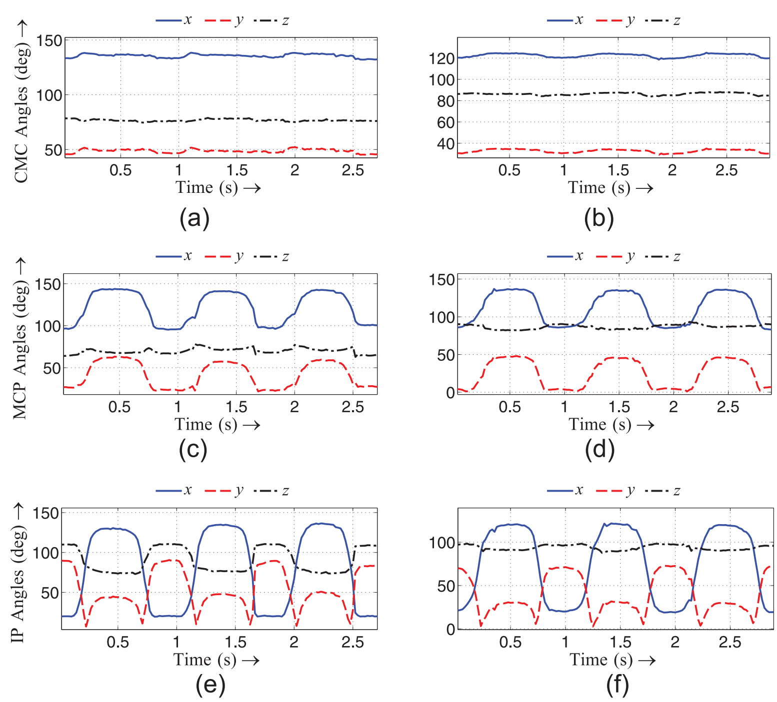

Fig. 12. Example trajectories from kinematic transparency tests without and with the exoskeleton for motion (d) at 1 Hz with Subject I. The left and right columns represent the plots of the various thumb phalanx angles with respect to the reference frame without and with the thumb exoskeleton, respectively.

trajectories without and with the exoskeleton. Correlation was used as a measure of transparency instead of root mean square error, as it is difficult for a subject to replicate exactly the same motion consistently with or without the device.

Table 4. Pearson's product moment correlation coefficient averaged over three repetitions, obtained from kinematic transparency tests. A Student's t distribution was used to compute p. The correlation is calculated only for those trajectories where significant motion was observed either with or without the exoskeleton.

Motion type	Carpometacarpal x	Carpometacarpal y	Carpometacarpal z	Metacarpophalangeal x	Metacarpophalangeal y	Metacarpophalangeal z	Interphalangeal x	Interphalangeal y	Interphalangeal z
(i)	0.9122 ($p < 0.01$)	0.9201 ($p < 0.01$)	0.5368 ($p < 0.01$)	0.9397 ($p < 0.01$)	0.7997 ($p < 0.01$)	0.4796 ($p < 0.01$)	0.9132 ($p < 0.01$)	0.6073 ($p < 0.01$)	0.5990 ($p < 0.01$)
(ii)	0.9077 ($p < 0.01$)	0.8874 ($p < 0.01$)	0.6727 ($p < 0.01$)	0.9414 ($p < 0.01$)	0.9071 ($p < 0.01$)	0.8293 ($p < 0.01$)	0.9383 ($p < 0.01$)	0.9277 ($p < 0.01$)	0.8375 ($p < 0.01$)
(iii)	0.9024 ($p < 0.01$)	0.8324 ($p < 0.01$)	0.6200 ($p < 0.01$)	0.9442 ($p < 0.01$)	0.6228 ($p < 0.01$)	0.6880 ($p < 0.01$)	0.9441 ($p < 0.01$)	0.5149 ($p < 0.01$)	0.7932 ($p < 0.01$)
(iv)	—	—	—	0.9658 ($p < 0.01$)	0.9582 ($p < 0.01$)	—	0.9677 ($p < 0.01$)	0.8852 ($p < 0.01$)	0.8139 ($p < 0.01$)

Results for motion (a) at 0.25 Hz showed that most of the thumb phalanx angle trajectories without and with the exoskeleton (Figure 9) were strongly correlated (Table 4) for the two phalanges and metacarpal of the thumb. Some deviation was observed in the trajectory of the angles about the z-axis for the phalanges. However, the range of motion about the z-axis was relatively small, compared with the other two axes. Results for motion (b) at 0.5 Hz also showed that the two sets of angle trajectories (Figure 10) were strongly correlated (Table 4). The range of motion at the CMC joint was relatively smaller with the exoskeleton than without it. This is because the wireform structure and the hook-and-loop fastener strap to hold the exoskeleton base on the hand occupy some space, which reduces the effective range. However, the nature of the motion was preserved, showing that the exoskeleton did not adversely affect the motion. The two sets of angle trajectories (Figure 11) were also strongly correlated (Table 4) for motion (c) at 0.75 Hz. The peaks of the motion with the exoskeleton plateaued for some of the trajectories. Also, some deviation was observed in the metacarpal trajectory about the z-axis and in the proximal and distal phalanges about the y- and z-axes for this motion. Finally, trajectories for motion (d) at 1 Hz also showed significant correlation (Table 4). Since, this motion involved only moving the MCP and IP joints in flexion–extension, little motion was observed at the CMC joint both without and with the exoskeleton (Figures 12(a) and 12(b)). This shows that the subject was able to move the MCP and IP joints with minimal motion at the CMC joint both without and with the exoskeleton. Some deviation was observed for the distal phalanx joint angle about the z-axis for this motion. It was also observed that it took slightly longer for the subject to complete the motion with the exoskeleton than without it, especially at higher frequencies. However, the nature of the trajectories was not significantly affected as the speed of motion increased, showing that the device does not alter the coordinated motion of the phalanges even at higher speeds. Similar results were obtained for the other subjects. Thus, these experiments demonstrate that, overall, the device preserves the natural motion of the thumb.

6.3. Torque control

Results from the first phase of the experiments showed that the joint torque controller could track the desired torque at the thumb exoskeleton joints with a root mean square error of 4.16% (0.0151 Nm), 13.07% (0.0294 Nm), 6.6% (0.0132 Nm) and 10.53% (0.0084 Nm) at the CMC FE, CMC AA, MCP, and IP joints, respectively (Figure 13). A relatively noisier torque output was observed at the CMC AA joint because a sliding-contact-type potentiometer was used at that joint for joint angle sensing (Section 3.5). Furthermore, the torque at each joint increased gradually as expected, owing to the sigmoid function (equation (10)). The torque envelope and mean torque required to move the four thumb joints were also determined for the four subjects (Figure 14).

Results from the second phase of the experiment showed that even when significant external disturbances were applied at the exoskeleton joints, which resulted in considerable changes in the exoskeleton joint angles (Figures 15(a) and 16(a)), the controller could maintain the desired torque level (Figures 15(b) and 16(b)). Thus, the device can perform torque control irrespective of the impedance of the external environment with which the exoskeleton is interacting.

7. Discussion

We carried out systematic design, control, and thorough experimental testing of a thumb exoskeleton. The novel thumb exoskeleton with Bowden-cable-based SEAs accomplishes the stated design objectives of accurate and stable bidirectional torque control of each thumb joint individually, kinematically compatible motion at the four thumb joints, a large workspace with the thumb and low weight, with the ability for free movement of the hand during device operation. Experiments with four human subjects showed that the device is capable of bidirectional torque control at each thumb joint individually. Kinematic transparency tests showed that the device is compatible with the natural motion at the four thumb joints. Experiments for evaluation of the workspace showed that the device provides a large workspace with the thumb (retains on average 85% of the thumb workspace). Finally, the Bowden-cable-based actuation mechanism with the use of selective laser sintering for manufacturing the prototype makes the design light in weight (≈136 g), while allowing free motion of the hand with minimal resistance.

A few limitations were observed during testing. During the kinematic transparency tests, even though the subjects were asked to keep their wrist joints stationary, some observable motion was present, especially for motions involving the CMC joint, as it was difficult for subjects to limit motion absolutely at the wrist joint in a timed trial. Any movement of the wrist joint would increase the range of motion, as the ground coordinate frame is determined using the markers on the wrist. This motion was more constrained with the exoskeleton than without, as an elastic band was wrapped around the wrist to keep the wireform structure in place. This might also have contributed to the slight reduction in the joint angles at the various joints during these experiments. The reduced range of motion with the exoskeleton in some regions was also partly due to the attachment interface connecting the exoskeleton to the thumb. While the wireform structure provides a good way to transfer forces to the thumb metacarpal, it restricts the motion at the CMC joint toward the palm to some extent. The hook-and-loop fastener straps at the middle and distal phalanx are close to each other and, therefore, reduce the range of motion at the distal joint. Moreover, the fastener strap that connects the exoskeleton base to the hand reduces the abduction–adduction range of motion to some extent. However, these effects are unavoidable.

Another limitation of the study is that only workspace is used as a measure of the range of motion with the device, as opposed to individual thumb joint range of motion. Measuring the range of motion accurately at the individual thumb joint when the device is donned is challenging, owing to the three-dimensional nature of the movement, nonorthogonal axes, and uncertain location of the joint center of rotation. Estimation of the individual thumb joint angles first requires estimation of the subject-specific parameters of the three-dimensional thumb exoskeleton model in vivo. Estimation of the thumb CMC joint parameters using a motion capture system has shown a large variability in the estimated parameters (Chang and Pollard, 2008). This might be because of the nonlinear nature of the underlying objective function being optimized to obtain these unknown parameters. Furthermore, the problem becomes significantly more challenging when using our exoskeleton, owing to frequent occlusion of the motion capture markers and large deformations of the flesh on the palmar side, if markers are placed on that side. Thus, we used the gross volume of the overall movement as a measure of the achievable workspace with the exoskeleton and compared it with the workspace volume without the exoskeleton. Furthermore, a limitation of using a convex hull to measure the volume of the workspace

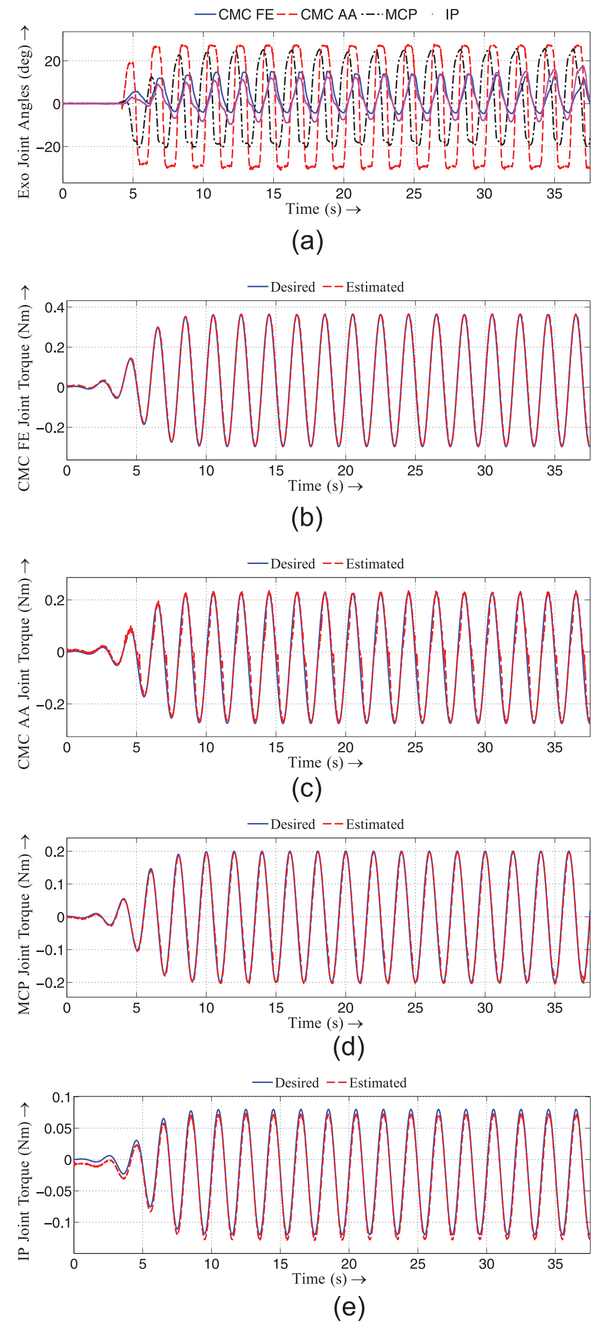

Fig. 13. Joint torque tracking performance at thumb exoskeleton joints for Subject 1. (a) Exoskeleton joint angles; (b) torque at exoskeleton carpometacarpal (CMC) flexion–extension (FE) joint; (c) torque at exoskeleton carpometacarpal abduction–adduction (AA) joint; (d) torque at exoskeleton metacarpophalangeal (MCP) joint; (e) torque at exoskeleton interphalangeal (IP) joint.

is that it requires large amounts of motion capture data to capture the volume of the workspace accurately.

The torque control experiments showed that the device could control the torque even under significant external disturbance. Some reduction in the range of motion was also observed, owing to the deformation of the flesh over the

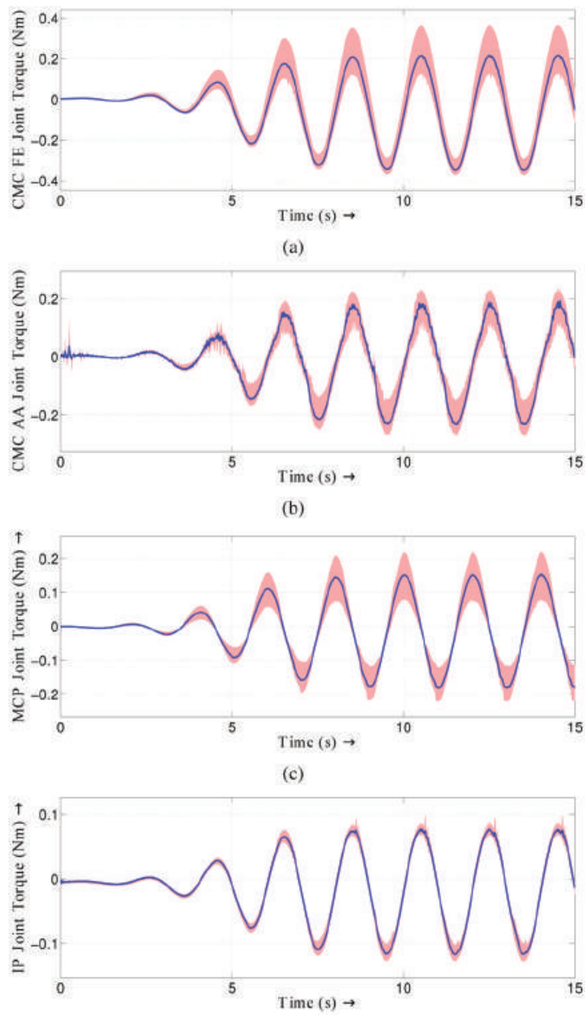

Fig. 14. Joint torque envelope (shaded region) and mean joint torque trajectory (solid line) at thumb exoskeleton joints for four subjects. (a) Torque at exoskeleton carpometacarpal (CMC) flexion–extension (FE) joint; (b) torque at exoskeleton carpometacarpal abduction–adduction (AA) joint; (c) torque at exoskeleton metacarpophalangeal (MCP) joint; (d) torque at exoskeleton interphalangeal (IP) joint. The joint torque envelope refers to the area between the maximum and minimum joint torque trajectories, considering the torque trajectories of the four subjects.

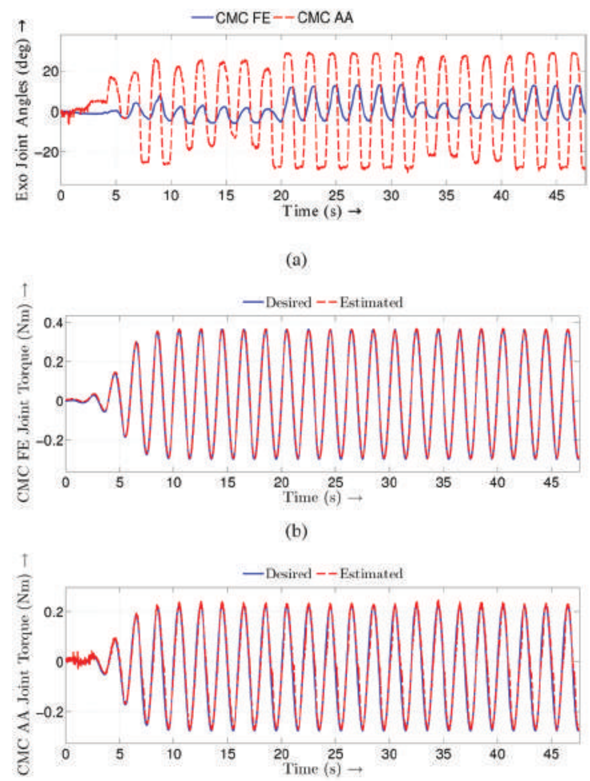

Fig. 15. Joint torque tracking performance at thumb exoskeleton carpometacarpal (CMC) joints when external disturbance is applied on the system for Subject 1. (a) Exoskeleton joint angles; (b) torque at the carpometacarpal flexion–extension (FE) exoskeleton joint; (c) torque at the carpometacarpal abduction–adduction (AA) exoskeleton joint.

metacarpal on the palmar side with the application of force on the wireform structure. The variation in torque between the subjects partly resulted from inherent differences in the requirement of torque for their thumbs and partly because the device was fitted to their hand at slightly shifted locations based on their hand contours. The device could also be driven in position control mode. We have implemented impedance control on the finger modules developed using similar Bowden-cable-based SEAs, which allowed us to render both low and high stiffness on the device and which is capable of tracking a trajectory in the high stiffness mode (Agarwal and Deshpande, 2015). In addition, our design allows for quick replacement of the compression springs of the SEAs without disconnecting the cables for further subject-specific customization.

All subjects reported that the device is light in weight and does not constraint their hand orientation. The subjects also reported that the low weight of the device makes it highly wearable and that it could be used for a long duration. Some subjects reported that the donning time of the device was long because of the number of fastener straps. One of the areas that still needs improvement before the device could be used in a clinical setting is the interface of the device with the hand. The current interface (especially the wireform structure) requires some subject-specific customization before it fits the hand of a subject at its natural position. In addition, we plan to improve the wearability of the device by attaching it to a glove that could help in quick donning and doffing of the device. Overall, the subjects reported that the interaction with the device felt comfortable and that it was effective in exercising their thumb.

In future, we plan to develop more advanced controllers (e.g. force-field control, assist-as-needed control) for the device to allow for more efficacious therapy regimens. One of the limitations of basic torque control over other

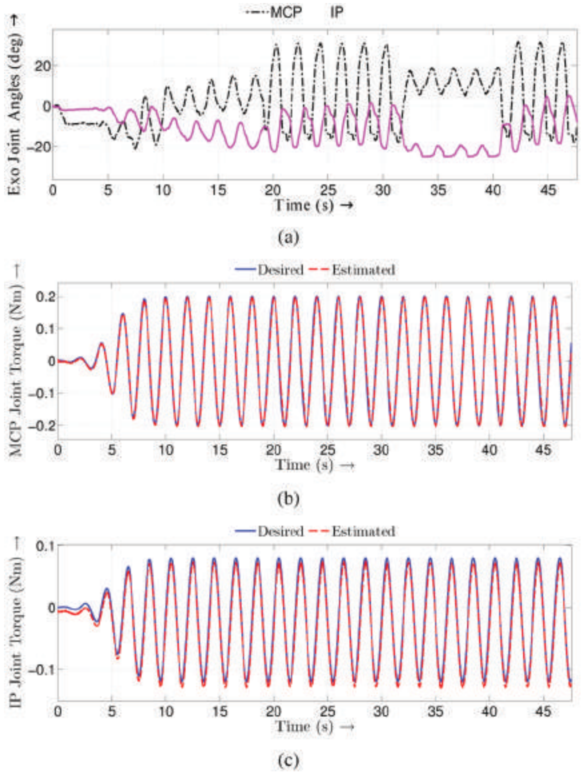

Fig. 16. The joint torque tracking performance at the thumb exoskeleton MCP and IP joints when external disturbance is applied on the system for Subject 1. (a) Exoskeleton joint angles, (b) torque at the MCP exoskeleton joint, and (c) torque at the IP exoskeleton joint.

advanced control paradigms is that it requires the torque required at each of the actuated joints to be specified explicitly for every subject. Some of the advanced controllers learn a subject-specific model of the coupled limb-exoskeleton system and automatically provide the required assistance to improve position-based tracking. However, the basis of these advanced controllers is torque control, which is therefore essential for their implementation. We plan to carry out experiments with a hand exoskeleton that assists the index and middle fingers and the thumb in the future. We also plan to carry out human subject studies with individuals who exhibit thumb pathologies to evaluate the efficacy of the device.

Funding

The author(s) disclosed receipt of the following financial support for the research, authorship, and/or publication of this article: This work was supported, in part, by the National Science Foundation (NSF) (grant number CNS-1135949) and the National Aeronautics and Space Administration (NASA) (grant number NNX12AM03G). The contents are solely the responsibility of the authors and do not necessarily represent the official views of the NSF or NASA.

References

Adamovich SV, Merians AS, Boian R, et al. (2005) A virtual reality-based exercise system for hand rehabilitation post-stroke. *Presence: Teleoperators and Virtual Environments* 14(2): 161–174.

Agarwal P and Deshpande AD (2015) Impedance and force-field control of the index finger module of a hand exoskeleton for rehabilitation. In: *IEEE international conference on rehabilitation robotics*, Singapore, 11–14 August 2015, pp.85–90. Piscataway, NJ: IEEE.

Agarwal P, Fox J, Yun Y, et al. (2015) An index finger exoskeleton with series elastic actuation for rehabilitation: Design, control and performance characterization. *International Journal of Robotics Research* 34(14): 1747–1772.

Aiple M and Schiele A (2013) Pushing the limits of the cybergrasp for haptic rendering. In: *IEEE international conference on robotics and automation*, Karlsruhe, Germany, 6–10 May 2013, pp.3541–3546. Piscataway, NJ: IEEE.

Avizzano CA, Bargagli F, Frisoli A, et al. (2000) The hand force feedback: Analysis and control of a haptic device for the human-hand. In: *IEEE international conference on systems, man, and cybernetics*, Nashville, TN, 8–11 October 2000, vol. 2, pp.989–994.

Beebe JA and Lang CE (2009) Active range of motion predicts upper extremity function 3 months after stroke. *Stroke* 40(5): 1772–1779.

Bernhardt M, Frey M, Colombo G, et al. (2005) Hybrid force-position control yields cooperative behaviour of the rehabilitation robot lokomat. In: *IEEE international conference on rehabilitation robotics*, Chicago, IL, 28 June–1 July 2005, pp.536–539. Piscataway, NJ: IEEE.

Bianchi M, Salaris P and Bicchi A (2013) Synergy-based hand pose sensing: Optimal glove design. *International Journal of Robotics Research* 32(4): 407–424.

Blank AA, French JA, Pehlivan AU, et al. (2014) Current trends in robot-assisted upper-limb stroke rehabilitation: promoting patient engagement in therapy. *Current Physical Medicine and Rehabilitation Reports* 2(3): 184–195.

Bouzit M, Burdea G, Popescu G, et al. (2002) The Rutgers Master II—new design force-feedback glove. *IEEE/ASME Transactions on Mechatronics* 7(2): 256–263.

Brault MW (2012) *Americans with Disabilities: 2010*. Washington, DC: US Department of Commerce, Economics and Statistics Administration, US Census Bureau.

Broeks JG, Lankhorst GJ, Rumping K, et al. (1999) The long-term outcome of arm function after stroke: Results of a follow-up study. *Disability and Rehabilitation* 21(8): 357–364.

Cai LL, Fong AJ, Otoshi CK, et al. (2006) Implications of assist-as-needed robotic step training after a complete spinal cord injury on intrinsic strategies of motor learning. *Journal of Neuroscience* 26(41): 10564–10568.

Cempini M, Cortese M and Vitiello N (2015) A powered finger–thumb wearable hand exoskeleton with self-aligning joint axes. *IEEE/ASME Transactions on Mechatronics* 20(2): 705–716.

Cerveri P, De Momi E, Lopomo N, et al. (2007) Finger kinematic modeling and real-time hand motion estimation. *Annals of Biomedical Engineering* 35(11): 1989–2002.

Chan RB and Childress DS (1990) On information transmission in human-machine systems: Channel capacity and optimal filtering. *IEEE Transactions on Systems, Man and Cybernetics* 20(5): 1136–1145.

Chang LY and Pollard NS (2008) Method for determining kinematic parameters of the in vivo thumb carpometacarpal joint. *IEEE Transactions on Biomedical Engineering* 55(7): 1897–1906.

Cheney W and Kincaid D (2009) *Linear Algebra: Theory and Applications*. Washington, DC: Saylor Foundation.

Choi J (2008) *Developing a 3-dimensional kinematic model of the hand for ergonomic analyses of hand posture, hand space envelope, and tendon excursion*. PhD Thesis, University of Michigan, USA.

Colombo R, Pisano F, Micera S, et al. (2005) Robotic techniques for upper limb evaluation and rehabilitation of stroke patients. *IEEE Transactions on Neural Systems and Rehabilitation Engineering* 13(3): 311–324.

Cooney WP, Lucca MJ, Chao E, et al. (1981) The kinesiology of the thumb trapeziometacarpal joint. *Journal of Bone & Joint Surgery* 63(9): 1371–1381.

DeSouza GN, Aubin P, Petersen K, et al. (2014) A pediatric robotic thumb exoskeleton for at-home rehabilitation: The isolated orthosis for thumb actuation (IOTA). *International Journal of Intelligent Computing and Cybernetics* 7(3): 233–252.

Dollar AM (2014) Classifying human hand use and the activities of daily living. In: Balasubramanian R and Santos VJ (eds) *The Human Hand as an Inspiration for Robot Hand Development*. Cham: Springer, pp.201–216.

Doolittle ND (1988) Stroke recovery: Review of the literature and suggestions for future research. *Journal of Neuroscience Nursing* 20(3): 169–173.

Fontana M, Fabio S, Marcheschi S, et al. (2013) Haptic hand exoskeleton for precision grasp simulation. *Journal of Mechanisms and Robotics* 5(4): 041014.

Gabiccini M, Stillfried G, Marino H, et al. (2013) A data-driven kinematic model of the human hand with soft-tissue artifact compensation mechanism for grasp synergy analysis. In: *IEEE/RSJ international conference on intelligent robots and systems*, Tokyo, Japan, 3–7 November 2013. pp.3738–3745. Piscataway, NJ: IEEE.

Garcia-Hernandez N, Sarakoglou I, Tsagarakis N, et al. (2014) Under-actuated hand exoskeleton with novel kinematics for potential use in rehabilitation. In: *EuroHaptics*, Versailles, France, 24–27 June 2014, pp.463–465. Berlin Heidelberg: Springer.

Harwin WS, Rahman T and Foulds RA (1995) A review of design issues in rehabilitation robotics with reference to North American research. *IEEE Transactions on Rehabilitation Engineering* 3(1): 3–13.

Hasegawa Y, Mikami Y, Watanabe K, et al. (2008) Five-fingered assistive hand with mechanical compliance of human finger. In: *IEEE international conference on robotics and automation*, Pasadena, CA, 19–23 May 2008, pp.718–724. Piscataway, NJ: IEEE.

Jo I and Bae J (2015) Design and control of a wearable hand exoskeleton with force-controllable and compact actuator modules. In: *IEEE international conference on robotics and automation*, Seattle, WA, 26–30 May 2015, pp.5596–5601. Piscataway, NJ: IEEE.

Kawasaki H, Kimura H, Ito S, et al. (2006) Hand rehabilitation support system based on self-motion control, with a clinical case report. In: *World automation congress*, Budapest, Hungary, 24–26 July 2006, pp. 1–6. Piscataway, NJ: IEEE.

Klein J, Spencer SJ and Reinkensmeyer DJ (2012) Breaking it down is better: Haptic decomposition of complex movements aids in robot-assisted motor learning. *Transactions on Neural Systems and Rehabilitation Engineering* 20(3): 268–275.

Lambercy O, Schröder D, Zwicker S, et al. (2013) Design of a thumb exoskeleton for hand rehabilitation. In: *Proceedings of the 7th international convention on rehabilitation engineering and assistive technology*, Gyeonggi-do, South Korea, 29–31 August 2013, paper no. 41. Singapore: Singapore Therapeutic, Assistive & Rehabilitative Technologies (START) Centre.

Leonardis D, Barsotti M, Loconsole C, et al. (2015) An EMG-controlled robotic hand exoskeleton for bilateral rehabilitation. *IEEE Transactions on Haptics* 8(2): 140–151.

Li J, Zheng R, Zhang Y, et al. (2011) iHandRehab: An interactive hand exoskeleton for active and passive rehabilitation. In: *IEEE international conference on rehabilitation robotics*, Zurich, Switzerland, 29 June–1 July 2011, pp.1–6. Piscataway, NJ: IEEE.

Li ZM and Tang J (2007) Coordination of thumb joints during opposition. *Journal of Biomechanics* 40(3): 502–510.

Lin HT, Kuo LC, Liu HY, et al. (2011) The three-dimensional analysis of three thumb joints coordination in activities of daily living. *Clinical Biomechanics* 26(4): 371–376.

Lotze M, Braun C, Birbaumer N, et al. (2003) Motor learning elicited by voluntary drive. *Brain* 126(4): 866–872.

Maeder-York P, Clites T, Boggs E, et al. (2014) Biologically inspired soft robot for thumb rehabilitation. *Journal of Medical Devices* 8(2): 020933-1-3.

Marchal-Crespo L and Reinkensmeyer DJ (2009) Review of control strategies for robotic movement training after neurologic injury. *Journal of Neuroengineering and Rehabilitation* 6(1): 20.

Meng W, Liu Q, Zhou Z, et al. (2015) Recent development of mechanisms and control strategies for robot-assisted lower limb rehabilitation. *Mechatronics* 31: 132–145.

Metcalf CD, Notley SV, Chappell PH, et al. (2008) Validation and application of a computational model for wrist and hand movements using surface markers. *IEEE Transactions on Biomedical Engineering* 55(3): 1199–1210.

Miyata N, Kouchi M, Kurihara T, et al. (2004) Modeling of human hand link structure from optical motion capture data. In: *IEEE/RSJ international conference on intelligent robots and systems*, Sendai, Japan, 28 September–2 October 2004, vol. 3, pp.2129–2135. Piscataway, NJ: IEEE.

Mozaffarian D, Benjamin EJ, Go AS, et al. (2015) Heart disease and stroke statistics—2015 update: a report from the American Heart Association. *Circulation* 131(4): e29.

Norton RL (1999) *Design of Machinery: An Introduction to the Synthesis and Analysis of Mechanisms and Machines*. Boston, MA: WCB McGraw-Hill.

Pehlivan A, Sergi F and O'Malley M (2014) A subject-adaptive controller for wrist robotic rehabilitation. *IEEE/ASME Transactions on Mechatronics* 20(3): 1338–1350.

Perez MA, Lungholt BK, Nyborg K, et al. (2004) Motor skill training induces changes in the excitability of the leg cortical area in healthy humans. *Experimental Brain Research* 159(2): 197–205.

Sale P, Lombardi V and Franceschini M (2012) Hand robotics rehabilitation: feasibility and preliminary results of a robotic treatment in patients with hemiparesis. *Stroke Research and Treatment* 2012: 820931.

Santos VJ and Valero-Cuevas FJ (2006) Reported anatomical variability naturally leads to multimodal distributions of Denavit–Hartenberg parameters for the human thumb. *IEEE Transactions on Biomedical Engineering* 53(2): 155–163.

Sarakoglou I, Tsagarakis NG and Caldwell DG (2004) Occupational and physical therapy using a hand exoskeleton based exerciser. In: *2004 IEEE/RSJ international conference on intelligent robots and systems*, Sendai, Japan, 28 September–2 October 2004, vol. 3, pp.2973–2978. Piscataway, NJ: IEEE.

Schabowsky CN, Godfrey SB, Holley RJ, et al. (2010) Development and pilot testing of HEXORR: hand exoskeleton rehabilitation robot. *Journal of Neuroengineering Rehabilitation* 7(1): 36.

Schmidt RA and Bjork RA (1992) New conceptualizations of practice: Common principles in three paradigms suggest new concepts for training. *Psychological Science* 3(4): 207–217.

Sheridan TB and Ferrell WR (1974) *Man-Machine Systems: Information, Control, and Decision Models of Human Performance*. Cambridge, MA: MIT.

Smith C (2008) Hand tools. Available at: http://www.ergonomics4schools.com/lzone/tools.htm (accessed 28 June 2016).

Smutz WP, Kongsayreepong A, Hughes RE, et al. (1998) Mechanical advantage of the thumb muscles. *Journal of Biomechanics* 31(6): 565–570.

Soucacos P (2001) Indications and selection for digital amputation and replantation. *Journal of Hand Surgery (British and European Volume)* 26(6): 572–581.

Sukal TM, Ellis MD and Dewald JP (2007) Shoulder abduction-induced reductions in reaching work area following hemiparetic stroke: neuroscientific implications. *Experimental Brain Research* 183(2): 215–223.

Takagi M, Iwata K, Takahashi Y, et al. (2009) Development of a grip aid system using air cylinders. In: *IEEE international conference on robotics and automation*, Kobe, Japan, 12–17 May 2009, pp. 2312–2317. Piscataway, NJ: IEEE.

Ueki S, Kawasaki H, Ito S, et al. (2012) Development of a hand-assist robot with multi-degrees-of-freedom for rehabilitation therapy. *IEEE/ASME Transactions on Mechatronics* 17(1): 136–146.

Villafañe JH, Cleland JA and Fernandez-De-Las-Penas C (2013) The effectiveness of a manual therapy and exercise protocol in patients with thumb carpometacarpal osteoarthritis: a randomized controlled trial. *Journal of Orthopaedic & Sports Physical Therapy* 43(4): 204–213.

Wang F, Shastri M, Jones CL, et al. (2011) Design and control of an actuated thumb exoskeleton for hand rehabilitation following stroke. In: *IEEE international conference on robotics and automation*, Shanghai, China, 9–13 May 2011, pp.3688–3693. Piscataway, NJ: IEEE.

Wikipedia (2016) Selective laser sintering. Available at: https://en.wikipedia.org/wiki/Selective_laser_sintering (accessed 25 January 2016).

Williams LS, Weinberger M, Harris LE, et al. (1999) Development of a stroke-specific quality of life scale. *Stroke* 30(7): 1362–1369.

Wissel J, Schelosky LD, Scott J, et al. (2010) Early development of spasticity following stroke: A prospective, observational trial. *Journal of Neurology* 257(7): 1067–1072.

Zhang X, Lee SW and Braido P (2003) Determining finger segmental centers of rotation in flexion–extension based on surface marker measurement. *Journal of Biomechanics* 36(8): 1097–1102.